Controlling mode orientations and frequencies in levitated cavity optomechanics

A. Pontin, H. Fu, J. H. Iacoponi, P. F. Barker, and T. S. Monteiro*
Department of Physics and Astronomy, University College London, Gower Street, WC1E 6BT London, United Kingdom

(Received 7 June 2022; accepted 12 December 2022; published 12 January 2023)

Cavity optomechanics offers quantum ground state cooling, control and measurement of small mechanical oscillators. However optomechanical backactions disturb the oscillator motions: they shift mechanical frequencies and, for a levitated oscillator, rotate the spatial orientation of the mechanical modes. This introduces added imprecisions when sensing the orientation of an external force. For a nanoparticle trapped in a tweezer in a cavity populated only by coherently scattered (CS) photons, we investigate experimentally mode orientation, via the $S_{xy}(\omega)$ mechanical cross-correlation spectra, as a function of the nanoparticle position in the cavity standing wave. We show that the CS field rotates the mechanical modes in the opposite direction to the cavity backaction, canceling the effect of the latter. It also opposes optical spring effects on the frequencies. We demonstrate a cancellation point, where it becomes possible to lock the modes near their *unperturbed* orientations and frequencies, independent of key experimental parameters, while retaining strong light-matter couplings that permit ground state cooling. This opens the way to sensing of directionality of very weak external forces, near quantum regimes.

DOI: 10.1103/PhysRevResearch.5.013013

I. INTRODUCTION

There is currently intense interest in sensing of ultraweak accelerations and forces using levitated nanoparticles [1], with several demonstrations to date of sensitivities ranging from the atto to zeptoNewton range [2–5] among others. Some of the work is directly motivated by the search for dark matter [6,7] and the importance of directionality [8] in this context. These experiments rely on some cooling for added stability and sensitivity. In parallel, optical cooling of levitated nanoparticles, both with cavities as well as active feedback methods [1] has led to dramatic progress, with quantum ground-state cooling of the center of mass recently achieved with an optical cavity [9] as well as with feedback cooling and quantum control [10,11]. Thus there is the real prospect measurements at or near quantum limited sensing regimes.

Quantum cooling with cavities was achieved with the introduction of the coherent scattering (CS) setup to levitated cavity optomechanics [12,13] using methods adapted from atomic physics [14–18]. In contrast to previous experiments, here the cavity is driven solely by the dipole radiation of an optically trapped silica particle. The nanoparticle is trapped at the focus of an optical tweezer along the z axis; the tweezer laser polarization angle and waist set the orientation and frequencies $\omega_x^{(0)}$, $\omega_y^{(0)}$, of the unperturbed motions, in the x-y plane. The CS setup yielded unprecedentedly high optomechanical coupling rates g_x, g_y, allowing quantum cooling. However, unavoidably, significant light-matter backaction effects are also observed.

Previous analysis [19,20] showed that x-y hybridization results from both cavity mediated, back action terms as well as an effective direct coupling. There can even be strong three-way hybridization of the normal modes in the x-y plane with optical modes, in strong-coupling regimes. The strong-coupling regime can even lead to the formation of dark and bright modes [20–22] that can impede cooling. While hybridization phenomena are seen in other setups (e.g., membranes), for the levitated optomechanics, they represent a change in *orientation* of the motional modes, so are of singular importance for applications such as directional force sensing.

Here we investigate measurement and control of the orientation of mechanical modes in the x-y plane experimentally by measuring cross-correlation $S_{xy}(\omega)$ spectra. In Ref. [23], it was shown that a directional force gives a characteristic spectral shape in $S_{xy}(\omega)$. However, misalignments between normal modes and detectors can mask the signal of a weak directional external force so it is important to suppress them. The setup is illustrated in Fig. 1. We show that rotation of the modes by an angle $\Phi_{\rm dyn}$ due to a dynamical optical backaction term is, away from the node, opposed by a rotation $\Phi_{\rm CS}$ due to the CS potential. In addition we find here, for the first time, that the experimental mechanical frequency shifts directly mirror this behavior. At the node, the optical spring effect due to the cavity dynamics softens the mechanical frequencies; away from the node, the CS potential stiffens the mechanical frequency. The two effects cancel at the same point as the cancellation of the mode rotation angle. At this point, the mechanical x, y frequencies both return to their unperturbed values and the modes are locked to their unperturbed orientation, for arbitrary input power and polarization. Yet, as

*Corresponding author: t.monteiro@ucl.ac.uk

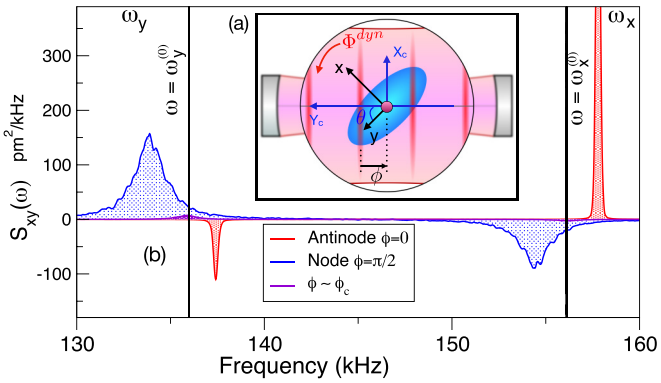

FIG. 1. (a) Inset illustrates a nanoparticle, trapped by an optical tweezer with x-y mechanical modes. The presence of a surrounding cavity, required for quantum cooling, hybridizes the modes and shifts their unperturbed frequencies $\omega_{x,y}^{(0)}$. The experimental tweezer polarization sets an initial angle θ between the x-y modes and cavity axis. Then, the optomechanical cavity hybridization dynamics adds an effective mode rotation $\Phi_{\rm dyn}$. However, away from optical nodes, the CS field opposes this effect. (b) We investigate mode orientation by measuring cross-correlation spectra $S_{xy}(\omega)$ for $\theta \simeq \pi/4$ as the trapping position is swept from node (blue, $\phi = \pi/2$) to near the antinode (red, $\phi = 0$) of the cavity standing wave. The x-y motions are always anticorrelated (peaks of opposite sign), but S_{xy} flips sign at $\phi = \phi_c$ [purple line, $S_{xy}(\omega) \sim 0$]. For this value, the CS field cancels $\Phi_{\rm dyn}$: the mechanical modes are locked at their unperturbed orientations *and* unperturbed frequencies for arbitrary power and θ, but can still be strongly cooled. The results have implications for directional force sensing and, in strong coupling regimes, the suppression of dark/bright modes.

discussed below, there is still strong optomechanical coupling that would, in principle, permit cavity cooling to the ground state in these regimes.

In Sec. II we review the experimental setup and in Sec. III the corresponding 2D Hamiltonian. In Sec. IV, we introduce the cross-correlations. In Sec. V, we discuss the experimental results. Finally, in Sec. VI, we discuss the results and present our conclusions.

II. EXPERIMENTAL SETUP

A schematic overview of the experiment is shown in Fig. 2(c). We use two Nd:YAG lasers at a wavelength $\lambda = 1064$ nm. A weak field from the first is used to implement a Pound-Drever-Hall (PDH) scheme to lock it to a high finesse Fabry-Perot cavity. The second laser illuminates an optical tweezer composed of a single aspheric lens of nominal numerical aperture $NA = 0.77$ and a symmetric condenser lens. The tweezer assembly is monolithic, is mounted on a three-axis translational stage and includes an aspheric collection lens of $NA = 0.3$, oriented at 90° from the propagation direction, which is exploited for imaging purposes. The tweezer trapping region is positioned at the center of the optical cavity which has a length $L_{\rm cav} = 12.23 \pm 0.02$ mm, a finesse $\mathcal{F} \simeq 31\,000$ (linewidth $\kappa/2\pi = 396 \pm 2$ kHz, input rate $\kappa_{\rm in}/2\pi = 162 \pm 2$ kHz) and a waist of 61 μm. The two lasers are phase offset locked by monitoring their beat note and their frequency separation is set to one free spectral range (FSR $= c/2L_{\rm cav} = 12.26 \pm 0.02$ GHz). The PDH beam is locked at resonance and the detuning of the trapping beam can be finely controlled. Importantly, the PDH beam is orthogonally polarized with respect to the tweezer beam and interacts with the particle only dispersively. This, in combination with the low power makes the role of the PDH beam in the dynamics negligible. The motion of the particle in the tweezer polarization plane is monitored by distributing the tweezer light collected by the condenser lens to two balanced detectors. Each detector is balanced using D-shaped mirrors oriented parallel and perpendicular to the beam polarization thus sensitive to x and y, respectively. The two detectors can measure independently the x and y motion with a rejection ratio potentially exceeding −30 dB, however, any imperfections in the orientations of the D mirror can result in a small mixing of x and y in the detected signals.

III. EFFECTIVE 2D HAMILTONIAN

In a coherent scattering (CS) approach, the optical cavity is not externally driven but it is populated exclusively by light scattered by the nanoparticle. The corresponding Hamiltonian results from the coherent interference between the electric fields of the tweezer and cavity $\hat{H} = -\frac{\alpha}{2}|\hat{\mathbf{E}}_{\rm cav} + \hat{\mathbf{E}}_{\rm tw}|^2$, where α is the polarizability of the nanosphere. The interference term $\propto (\hat{\mathbf{E}}_{\rm cav}^\dagger \hat{\mathbf{E}}_{\rm tw} + \hat{\mathbf{E}}_{\rm cav}\hat{\mathbf{E}}_{\rm tw}^\dagger)$ gives rise to an effective CS potential:

$$\hat{V}_{\rm CS}/\hbar = -E_d \cos(\phi + k\hat{Y}_c) e^{-(\hat{x}^2/w_x^2 + \hat{y}^2/w_y^2)}[\hat{a} + \hat{a}^\dagger]. \quad (1)$$

In the above, we omitted the $\hat{z}$ dependence. The CS dynamics decouples into a $2+1$ dynamics with x-y motion close in frequency and prone to hybridize; and a (typically) off-resonant z motion that is largely decoupled. We note that the z motion can be strongly cooled using feedback cooling [10,11] but, in most experimental implementations, z is anyway moderately cooled due to a small unavoidable tilt relative to the cavity z axis. As a check, the effect of the tilt and the full z dynamics is taken into account in numerical simulations but is not included in the discussion as the 2D model was found to be quite accurate.

In Eq. (1), Y_c represents the cavity axis. Relating the cavity coordinates to the tweezer frame is a simple rotation of the coordinate frames $[X_c \;\; Y_c]^T = R_z(\theta)[x \;\; y]^T$, where $R_z(\theta)$ is the 2D rotation matrix. ϕ is the displacement of the trap from an antinode, $w_y \simeq 1.068$ μm and $w_x \simeq 0.928$ μm are the tweezer waists. Linearized equations of motion are obtained using Eq. (1); operators are expanded about equilibrium values, thus the optical field operators $\hat{a} \to \overline{\alpha} + \hat{a}(t)$ are expanded about the mean field, where $n_p = |\overline{\alpha}|^2$ is the mean photon occupancy of the cavity.

The linearization yields, for the conservative part of the dynamics,

$$\frac{\hat{H}_{\rm CS}}{\hbar} = \Delta\hat{a}^\dagger\hat{a} + \sum_{j=x,y} \omega_j \hat{b}_j^\dagger \hat{b}_j + (g_x\hat{x} + g_y\hat{y})(\hat{a} + \hat{a}^\dagger) + g_{xy}\hat{x}\hat{y}. \quad (2)$$

Hence there are typical coupling terms $g_x\hat{x}(\hat{a} + \hat{a}^\dagger)$ and $g_y\hat{y}(\hat{a} + \hat{a}^\dagger)$. However, away from the node, the CS potential also yields direct coupling terms $g_{xy}\hat{x}\hat{y}$ that are of similar order to the usual linearized terms, thus do not vanish as the

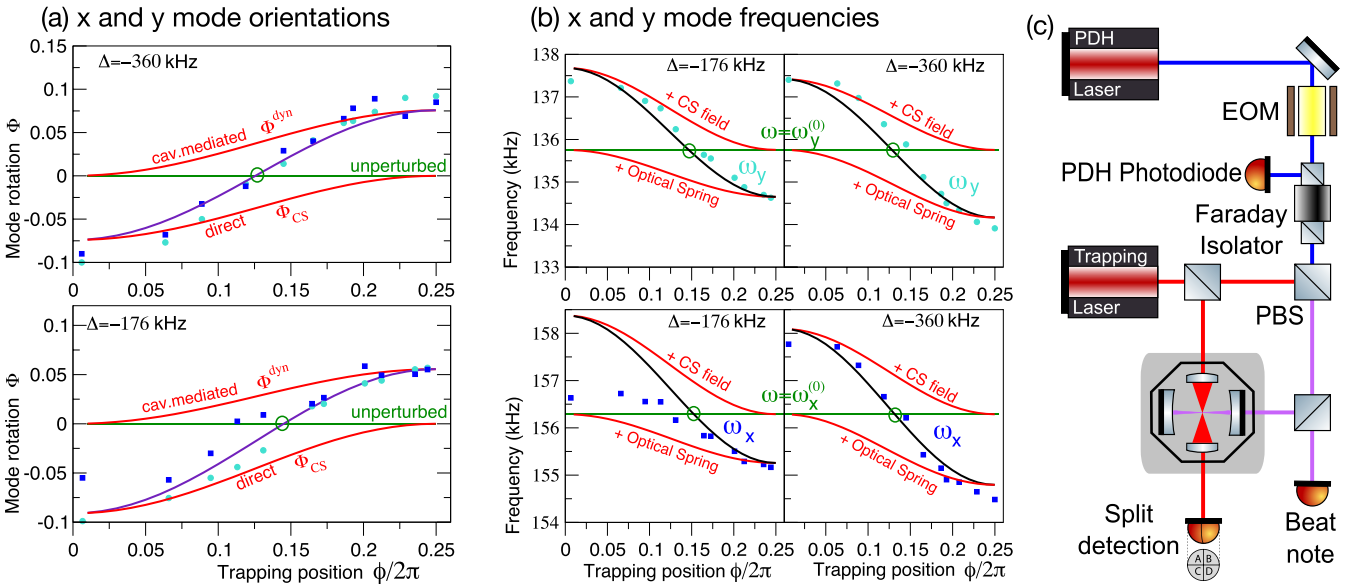

FIG. 2. (a) Measured orientation of the mechanical modes in x-y plane as a function of trapping position. The mode rotation angles Φ are obtained from experimental cross-correlation spectra, $S_{xy}(\omega)$: squares (blue) correspond to the x peak, circles (cyan) to the y peak. Φ combines a positive sign contribution $\Phi_{\rm dyn}$, from the optomechanical dynamics arising from optical backaction, and $\Phi_{\rm CS}$, a negative sign contribution from the static CS field. $\Phi_{\rm dyn}$ is dominant at the node ($\phi = \pi/2$), while $\Phi_{\rm CS}$ dominates at the antinode ($\phi = 0$). Where they cancel (green circle, $\phi = \phi_c$) the rotation becomes zero. The measured values of Φ are compared with $\Phi_{\rm CS} + \Phi_{\rm dyn}$ calculated from theory (violet lines). (b) Shows that the frequency behavior mirrors the mode rotation behavior: the optomechanical optical spring effect softens the mechanical frequencies for red detuning, while in contrast CS field stiffens the frequencies. At $\phi \simeq \phi_c$, the two contributions cancel, leaving only the unperturbed mechanical frequency set by the tweezer trap. Red lines denote theoretical values, calculated from linearized optomechanical equations of motion. Black line shows their combined effect. $\theta \simeq \pi/4$ for all plots. (c) Experimental setup, described in the text.

quantum occupancies are approached. Details are given in the Appendix and Ref. [19].

IV. CROSS-CORRELATION SPECTRA $S_{xy}(\omega)$

Provided hybridization is moderate, x-y hybridization may be modelled as a correction to the 1D unhybridized solutions;

$$\begin{aligned}\hat{x}(\omega) &\simeq \hat{x}^{1D}(\omega) + \mathcal{R}_{xy}(\omega)\hat{y}(\omega),\\ \hat{y}(\omega) &\simeq \hat{y}^{1D}(\omega) + \mathcal{R}_{yx}(\omega)\hat{x}(\omega),\end{aligned} \tag{3}$$

where $\mathcal{R}_{xy}, \mathcal{R}_{yx}$ are hybridization functions. In that case if $\mathcal{R}_{xy} \simeq -\mathcal{R}_{yx}$, the above linear x-y hybridization relation is already suggestive of a simple frame rotation.

One can then readily show (see Appendix for details) that the resulting symmetrized mechanical cross-correlation spectra

$$S_{xy}(\omega) = \tfrac{1}{2}(\langle[\hat{x}]^\dagger\hat{y}\rangle + \langle[\hat{y}]^\dagger\hat{x}\rangle) \tag{4}$$

correspond to

$$S_{xy}(\omega) \approx \mathrm{Re}(\mathcal{R}_{yx}(\omega))S_{xx}(\omega) + \mathrm{Re}(\mathcal{R}_{xy}(\omega))S_{yy}(\omega) \tag{5}$$

and depend on the real parts of the hybridization functions. Hence we can write

$$S_{xy}(\omega) \simeq \Phi\,[S_{yy}(\omega) - S_{xx}(\omega)]. \tag{6}$$

The above expression is generic to a 2D optomechanical system in many typical regimes. It shows that the cross-correlation PSDs may be readily related to the usual displacement PSDs by a simple numerical scaling constant that corresponds to the mode rotation angle Φ.

A. Calculating the rotation angle Φ

For the CS setup investigated here, we can obtain explicit analytical forms for the hybridization function $\mathcal{R}_{xy}(\omega)$. For $\omega \sim \omega_{x,y}$, one can show $\mathcal{R}_{xy} \simeq -\mathcal{R}_{yx} \equiv G(\omega)/(\omega_x - \omega_y)$, where $G(\omega) = [i\eta_c(\omega)g_x g_y + g_{xy}]$ and $\eta_c = \chi(\omega) - \chi^*(-\omega)$, $\chi(\omega) = 1/(-i(\omega+\Delta)+\kappa/2)$ is the cavity susceptibility function [19,20].

The angle $\Phi = \Phi_{\rm dyn} + \Phi_{\rm CS}$ can thus be decomposed into two separate contributions: (i) a cavity mediated term $\Phi_{\rm dyn} \equiv \mathrm{Re}(i\eta_c g_x g_y)/(\omega_x - \omega_y)$ and (ii) a direct contribution $\Phi_{\rm CS} \equiv g_{xy}/(\omega_x - \omega_y)$ arising from the static CS potential. It was found in Ref. [19] that the optomechanical couplings are $g_x \simeq -E_d\, k \sin\theta \sin\phi X_{zpf}$, $g_y \simeq -E_d\, k \cos\theta \sin\phi Y_{zpf}$ and

$$g_{xy} \simeq g_x g_y 2\Delta \cot^2\phi/(\kappa^2/4 + \Delta^2) \tag{7}$$

thus the combined dynamical and CS rotation becomes

$$\Phi = \Phi_{\rm dyn} + \Phi_{\rm CS} = \frac{g_x g_y}{(\omega_x - \omega_y)}\left[\mathrm{Re}(i\eta_c) + \frac{2\Delta\cot^2\phi}{(\kappa^2/4+\Delta^2)}\right]. \tag{8}$$

The two terms are of the opposite sign, hence their effect is to rotate the modes in opposing directions. $X_{zpf} = \sqrt{\hbar/(2m\omega_x)}$, $Y_{zpf} = \sqrt{\hbar/(2m\omega_y)}$.

V. ANALYSIS OF THE EXPERIMENTS

The experimental PSDs S_{xx}, S_{yy} and correlation spectra at different trap positions are acquired at a constant pressure of 3×10^{-3} mbar with each time trace covering an observation time of 10 s. From these we obtain Φ as a function of the trapping positions ϕ by directly exploiting Eq. (6). That is, we take the difference of the measured motional PSDs S_{xx}, S_{yy} and find the single scaling constant which best reproduces the experimentally measured $S_{xy}(\omega)$.

The measured rotation in the mode orientations are shown in Fig. 2(a) for two separate detunings which represent the two interesting limit cases. To model the experiments, for all results, we employed nanosphere radius $R = 60.1$ nm, input power to the tweezer $P_{tw} = 0.485$ W and $\theta = 49^\circ$.

Behavior of the mechanical frequencies. An interesting and unexpected observation is that the behavior of the frequencies mirrors the mode rotations; at the $\phi \simeq \phi_c$ position, they return to their unperturbed values. This is shown in Fig. 2(b), for two values of the optical detuning. Here, the experimental values are obtained by fitting the PSDs.

The unperturbed mechanical frequencies of this levitated optomechanical system are set by the tweezer trap:

$$\left(\omega^{(0)}_{(x,y)}\right)^2 = \frac{\alpha \epsilon^2_{tw}}{m w^2_{x,y}}, \tag{9}$$

where $\epsilon^2_{tw} = 4P_{tw}/(w_x w_y \pi c \epsilon_0)$ is related to the input power from the tweezer. In the presence of the cavity the coupling to the optical mode dynamics introduces an optical spring "softening" (for red-detuned light) that is generic to all cavity optomechanical setups. In strong coupling regimes, this can be a very large shift. Neglecting a correction for 2D x-y coupling [19,20], the optical spring shift $(\delta\omega^{(j)}_{OS})^2 = \mathrm{Re}(-i2g^2_j\omega^{(0)}_j\eta_c)$ with $j = x, y$.

However, for the coherent scattering setup, there is a countervailing potential, obtained by linearizing Eq. (1), that "stiffens" the mechanical frequencies. It is a static contribution, dependent on the mean photon occupancy of the cavity, thus can be considered an effect of cotrapping by the CS field. It takes the form $(\delta\omega^{(j)}_{\mathrm{CS}})^2 \simeq -(E_d k^2 \sin^2\theta/m)2\Delta\cos^2\phi[(\kappa/2)^2 + \Delta^2]^{-1}$.

Hence the corrected frequencies combine the two contributions: $(\omega_j)^2 = (\omega^{(0)}_j)^2 + (\delta\omega^{(j)}_{\mathrm{CS}})^2 + (\delta\omega^{(j)}_{OS})^2$ and may be written

$$(\omega_j)^2 \simeq \left(\omega^{(0)}_j\right)^2 - 2g^2_j\omega^{(0)}_j\left[\mathrm{Re}(i\eta_c) + \frac{2\Delta\cot^2\phi}{(\kappa^2/4 + \Delta^2)}\right]. \tag{10}$$

It is clear from a comparison with Eq. (8) that the multiplicative terms in square brackets are equivalent; thus if they cancel for the mode orientations, they cancel for the frequency contributions. A more refined analysis, with consideration of weaker corrections and higher order terms will show that the $\phi = \phi_c$ point is not identical for the frequencies and orientations, but it is quite close.

In Fig. 3(a), the procedure for measuring the mode angles Φ as a function of ϕ is further illustrated. A small imperfection in the orientation of the D mirror, of the order of 2°, for the detection of x introduces a nonvanishing cross-correlation with y even in absence of the cavity induced rotation. This translates into a constant bias in the evaluation of Φ, which can be easily removed.

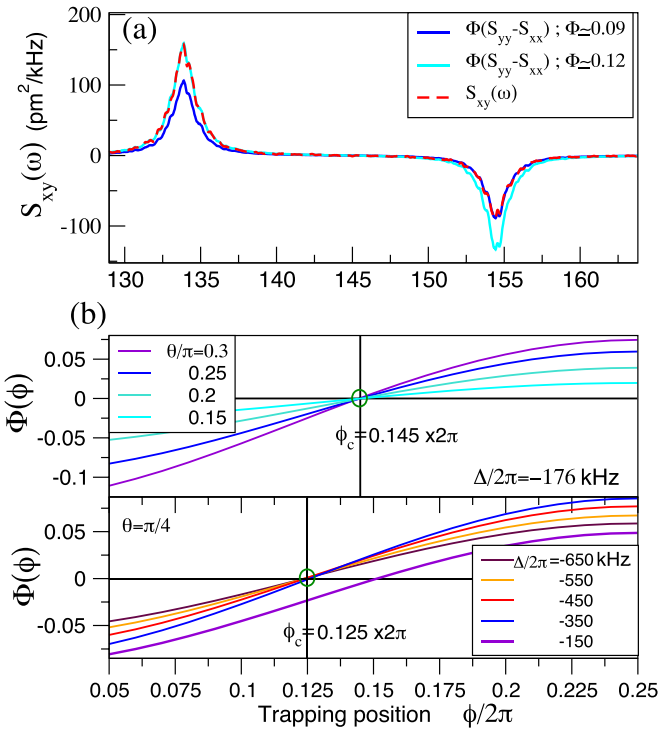

FIG. 3. (a) To measure mode rotation, we compare cross-correlation spectra $S_{xy}(\omega)$ with the rescaled difference between PSDs $S_{xy}(\omega) \simeq \Phi(\phi)\,[S_{yy}(\omega) - S_{xx}(\omega)]$ to extract $\Phi(\phi)$. Plots show experimental S_{xy} at a node, $\Delta/2\pi = -360$ kHz and rescaled, measured, $S_{yy} - S_{xx}$. The rescaling gives excellent agreement, but there is a bias $\Phi_\beta \approx 0.03$ arising from an imperfection in the orientation of the D mirror ($\sim 2^\circ$) for the x detector. This yields a systematic shift between the scaling of all points obtained from the y peak (lower frequency) and the x peak (higher frequency). In Fig. 2, all y (cyan) data points are shifted by a constant, $\Phi(\phi) \to \Phi(\phi) - \Phi_\beta$. Upper red curve shows x-y hybridization mediated by the cavity mode. (b) Illustrates the "locking" of the mode orientation at $\phi = \phi_c$. (i) (Top) For $\Delta/2\pi = -176$ kHz, nearing resonance at $\omega_{x,y}/(2\pi) \sim 150$ kHz, $\phi_c/2\pi = 0.145$. At this point, for arbitrary tweezer polarization θ or input power, the modes remain at the unperturbed orientations. (ii) (Bottom) For large detuning $-\Delta/2\pi > 350$ kHz, the locking point is $\phi_c/2\pi = 0.125$. For lower detunings, ϕ_c moves towards the node and at $\Delta/2\pi = -150$ kHz, $\phi_c/2\pi \simeq 0.15$.

A. Insensitivity of ϕ_c to key experimental parameters

The position of the cancellation point is shown in Fig. 3(b). Clearly, from Eqs. (8) and (10), there is no dependence of ϕ_c on the experimental polarization or input power. The upper panel shows this behavior for $\Delta/2\pi = -176$ kHz. The rate of rotation of the mode orientation varies considerably, but the cancellation point remains fixed at $\phi_c/2\pi = 0.145$. The lower panel shows that for large detuning, ϕ_c is independent of Δ. As shown in Ref. [19], at large detuning, $\mathrm{Re}(i\eta_c) \to \frac{-2\Delta}{(\kappa^2/4+\Delta^2)}$ is real, we obtain $1 - 2\cot^2\phi_c = 0$, implying $\phi_c/2\pi = 0.125$ for all Δ. However, at resonance ($-\Delta \sim \omega_{x,y}$), ϕ_c moves towards the node. For this particular cavity, $\phi_c/2\pi \simeq 0.15$ near resonance. For lower κ and below resonance, one can

approach $\phi_c/2\pi = 0.2$, if a lower cavity photon occupancy is desirable. However, as shown in Appendix for $\phi_c/2\pi \gtrsim 0.15$ the cross-correlations are progressively less strongly suppressed, resulting in a significant $S_{xy}(\omega) \neq 0$ residue.

In summary, for a given cavity and the CS setup, certain parameters (such as cavity finesse and thus mirror decay rate κ) are essentially fixed. The input power, θ and Δ are adjustable. The cancellation point is completely independent of the first two and independent of Δ if the detuning is larger (by about a factor of 2) than the mechanical frequencies.

VI. DISCUSSION AND CONCLUSIONS

A. Prospects for quantum cooling and sensing at cancellation points

To date several experiments have achieved cavity cooling to or near ground states, of one or both x-y mechanical modes [9,24,25]. The role of hybridization in 2D cavity cooling was investigated in Refs. [19,20]. In Refs. [9,24], the x-y modes became near degenerate in frequency, at the quantum cooling parameters. Hence, for [9], although $g_x \gg g_y$, the hybridization caused some cross-heating between the strongly cooled mode and the hot, more weakly coupled mode (the definition of x, y axes may vary for different setups but in our discussion the strongest coupled mode lies along the cavity axis). For $g_x \sim g_y$, this leads to the formation of dark-bright modes, where x-y–optical hybridization generates a "dark" mode that is not coupled to the light; and a more strongly coupled (and thus strongly cooled) "bright" mode. This impedes simultaneous cooling.

In Ref. [20], the *geometric* dark-bright modes characteristic of levitated optomechanics were introduced and investigated. For geometric dark-bright modes, the hybridization has a direct interpretation corresponding to the physical orientation of the hybridized x-y modes. The bright mode corresponds to the x mode aligning with the cavity axis, while the y axis becomes orthogonal. An analysis of the conditions for strong simultaneous cooling was given by a so called "Goldilocks" criterion that stipulates the coupling can be neither too large, nor too small:

$$\sqrt{\kappa\Gamma/8} \lesssim g \lesssim \sqrt{\kappa/(8\Gamma)}|\omega_y - \omega_x|, \tag{11}$$

where Γ can be loosely identified with the total motional heating rate (typically $\Gamma \sim \gamma_m n_B$ if background gas collisions are dominant). A more recent experiment [25] within the "Goldilocks" zone achieved 2D simultaneous cooling, with $n_x, n_y \sim 0.8$.

In the context of 2D cooling, operating at cancellation points introduces an advantageous feature (suppression of dark bright modes) and a disadvantageous feature (increase in phase noise). As clearly the formation of bright and dark modes corresponds to a mode rotation angle of $\Phi = \pi/4$, fully suppressing the mode rotation also impedes the formation of the dark mode. However, the present experiments are not in the sideband resolved regime (as κ is too large by about a factor of 2) and are not at very low pressures required for ground state cooling.

Moving away from the cavity node entails a larger cavity photon occupancy. Hence, to achieve ground state cooling, this imposes more stringent constraints on the technical noises influencing the dynamics, in particular laser frequency noise. For instance, without even attempting parameter optimization, if we consider the same parameters as the current experiment, with the exception of a cavity linewidth reduced by a factor 2 (i.e., $\kappa/2\pi \simeq 200$ kHz) a mean phonon occupation approaching 1 can be achieved for both x and y simultaneously in absence of frequency noise at a pressure of the order of 10^{-8} mbar. The mean phonon number increase due to classical phase noise can be estimated as $n_{\rm ph} = \frac{n_p}{\kappa}\frac{\Delta}{\omega_i} S_{\dot\phi\dot\phi}(\omega_i)$ [26,27], where n_p is the cavity photon occupation. Considering $\Delta/\omega_i \simeq 1$ and $S_{\dot\phi\dot\phi} \simeq 0.1$ Hz^2/Hz, i.e., the value reported in Ref. [9], one finds $n_{\rm ph} \simeq 10$ at the cancellation point. This indicates that an improvement on the classical phase noise slightly above an order of magnitude, compared to the current state-of-the-art of levitated experiments, will permit ground state cooling while taking full advantage of the modes locking. Such technical improvement is in principle achievable in future experiments.

B. Conclusions

For force sensing applications, ground state cooling is not a strict requirement. There is increasing interest in the sensing of the direction of weak external forces, motivated by a range of applications. For example, the directional sensitivity of levitated nanoparticles aids the search for dark matter candidates since rejection of background events can be enhanced by the knowledge of the direction of the incoming dark matter candidate [6–8]. A new proposal for sensing stochastic but directional external forces [23] via their—previously overlooked—ability to correlate the mechanical modes highlights the importance of controlling and stabilising mode orientations.

We demonstrated experimentally that, in addition to their already demonstrated effectiveness for quantum cooling, CS setups offer a unique means of controlling and mitigating errors in orientations of the mechanical modes. This was achieved by moving away from the usual configuration of trapping at a node of the cavity standing wave. For weak force sensing, the requirements for maximal quantum cooperativities are less stringent than in the search for macroscopic quantum coherence. In any case, CS setups employ far lower photon occupancies than standard dispersive setups, thus laser phase noises do not impede the directional sensing at near-quantum regimes. Cavity dynamics away from the node is also attracting increasing interest as it is necessary to cool rotational degrees of freedom [28,29]. In fact, the suppression of cavity back-actions away from the node can impede the formation of bright/dark modes in the strong coupling regime allowing efficient 2D quantum cooling [20]. In addition, it was found here that the frequency shifts precisely mirror this effect and that the cancellation point, for lower detunings, moves closer to the node.

ACKNOWLEDGMENTS

The authors would like to acknowledge helpful discussions with J. Gosling and M. Toroš. The authors acknowledge funding from the Engineering and Physical Sciences Research

Council (EPSRC) Grant No. EP/N031105/1. H.F. and J.H.I. acknowledge EPSRC studentship funding via Grants No. EP/L015242/1 (H.F.) and No. EP/R513143/1 (J.H.I.).

APPENDIX A: ADDITIONAL EXPERIMENTAL DETAILS

A 3D schematic overview of the core of the experiment is shown in Fig. 4(a). The tweezer field is linearly polarized along the y axis and propagates along the z axis, which coincides with Z_c. The cavity axis lies in the Y_c direction and its field is polarized along the X_c direction. In this setting, the transformation of the reference frames defined in the main text is simply given by a 3D rotation matrix around the z axis.

The split detection exploits D-shaped mirrors which cut the beam in two sections so that half is transmitted and half is reflected. The two halves are sent to individual photodiodes and the difference of the respective photocurrents acquired. This guarantees rejection of classical intensity noise by 30–40 dB, which is typically sufficient for a shot noise limited detection. The D mirrors are mounted on rotation mounts so that their orientation can be finely adjusted to achieve optimal rejection of x and y mixing in their respective detectors.

APPENDIX B: MECHANICAL FREQUENCIES

The combined tweezer-cavity Hamiltonian takes the form

$$\hat{H} = -\frac{\alpha}{2}|\hat{\mathbf{E}}_{\rm cav} + \hat{\mathbf{E}}_{\rm tw}|^2, \tag{B1}$$

where $\hat{\mathbf{E}}_{\rm cav}$ ($\hat{\mathbf{E}}_{\rm tw}$) denotes the cavity (tweezer) field, $\alpha = 3\epsilon_0 V_s \frac{\epsilon_R - 1}{\epsilon_R + 2}$ is the polarizability of the nanosphere, V_s is the volume of the nanosphere, ϵ_0 is the permittivity of free space, and ϵ_R is the relative dielectric permittivity.

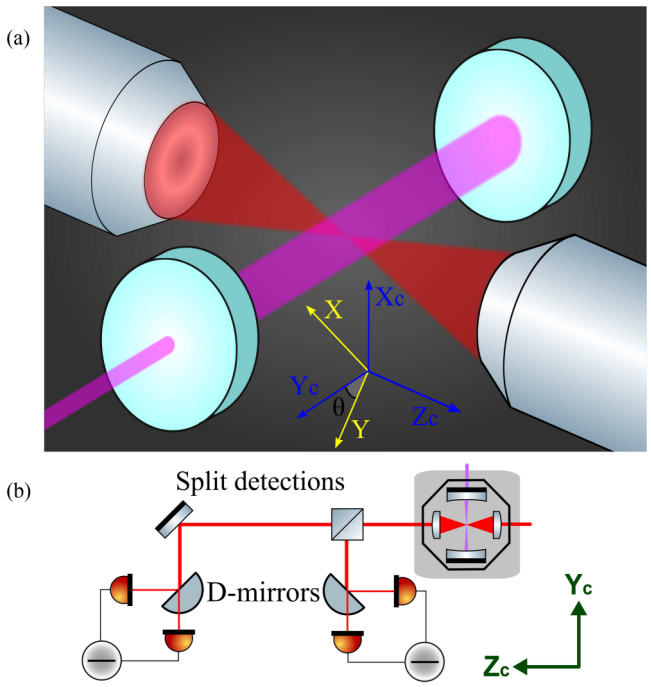

FIG. 4. (a) 3D schematic overview of the experimental setup highlighting the orientation of the tweezer and cavity field. (b) Optical layout of the split detection.

We assume a coherent Gaussian tweezer field and replace the modes with c numbers to find

$$\hat{\mathbf{E}}_{\rm tw} = \frac{\epsilon_{tw}}{2}\frac{1}{\sqrt{1+\left(\frac{z}{z_R}\right)^2}} e^{-\frac{\hat{x}^2}{w_x^2}} e^{-\frac{\hat{y}^2}{w_y^2}} e^{ik\hat{z}+i\Phi(\hat{z})} e^{-i\omega_{\rm tw}t}\mathbf{e}_y + \text{c.c.}, \tag{B2}$$

where $\Phi(z) = -\arctan\frac{z}{z_R}$ is the Gouy phase, $z_R = \frac{\pi w_x w_y}{\lambda}$ is the Rayleigh range, w_x (w_y) are the beam waist along the x (y) axis, $\epsilon_{tw} = \sqrt{\frac{4P_{\rm tw}}{w_x w_y \pi \epsilon_0 c}}$ is the amplitude of the electric field, c is the speed of light, $P_{\rm tw}$ is the laser power, $\omega_{\rm tw}$ is the tweezer angular frequency, t is the time, and $\hat{\boldsymbol{r}} = (\hat{x}, \hat{y}, \hat{z})$ is the position of the nanoparticle. $\mathbf{e}_j$ are the unit vectors: $\mathbf{e}_z$ is aligned with the symmetry axis of the tweezer field and $\mathbf{e}_y$ is aligned with the polarization of the tweezer field.

The cavity field is given by

$$\hat{\mathbf{E}}_{\rm cav} = \epsilon_c \cos\left(k\left(Y_0^{(c)} + \hat{Y}^{(c)}\right)\right)\mathbf{e}_x^c[\hat{a} + \hat{a}^\dagger], \tag{B3}$$

where $\epsilon_c = \sqrt{\frac{\hbar\omega_c}{2\epsilon_0 V_c}}$ is the amplitude at the center of the cavity, V_c is the cavity volume, ω_c is the cavity frequency, $\hat{a}$ ($\hat{a}^\dagger$)is the annihilation (creation) operator, $Y_0^{(c)}$ is an offset of the cavity coordinate system (centered at a cavity antinode) with respect to the tweezer coordinate system.

The cavity X_c-Y_c plane is rotated by an angle θ with respect to the tweezer x-y plane. For $\theta = 0$, the tweezer polarization (y axis) becomes aligned with the cavity symmetry axis (Y_c axis). In particular, we have $\hat{Y}^{(c)} = \sin(\theta)\hat{x} + \cos(\theta)\hat{y}$ while $\hat{X}^{(c)} = \cos(\theta)\hat{x} - \sin(\theta)\hat{y}$.

We expand the Hamiltonian in Eq. (B1), exploiting Eqs. (B2) and (B3) to obtain three terms:

$$\hat{H} = -\frac{\alpha}{2}|\hat{\mathbf{E}}_{\rm tw}|^2 - \frac{\alpha}{2}|\hat{\mathbf{E}}_{\rm cav}|^2 - \frac{\alpha\sin(\theta)}{2}(\hat{\mathbf{E}}_{\rm cav}^\dagger\hat{\mathbf{E}}_{\rm tw} + \hat{\mathbf{E}}_{\rm cav}\hat{\mathbf{E}}_{\rm tw}^\dagger), \tag{B4}$$

where the terms on the right hand-side represent the tweezer trapping potential, the cavity intensity field, and the tweezer-cavity interaction term (from left to right). The first (tweezer field) term dominates the trapping and primarily sets the three mechanical frequencies ω_x, ω_y, and ω_z. In the discussion below we focus only on the x, y modes.

The second term represents trapping by the cavity intensity potential. In earlier experiments in levitated cavity optomechanics with no tweezer trap, this field determined the mechanical frequencies. However, achieving reasonable frequencies required very high photon occupancies $n_p \sim 10^{10}$. In CS setups, this term provides a negligible correction to the frequencies but is included in the numerics for precision.

The third term, which we will denote as $\hat{V}_{\rm CS}$, is the most interesting, as this is the coherent scattering potential that has had a transformative effect in the levitated cavity optomechanics field:

$$\frac{\hat{V}_{\rm CS}}{\hbar} = -E_d\cos(\phi + k(\hat{x}\sin\theta + \hat{y}\cos\theta))e^{-\frac{\hat{x}^2}{w_x^2}} e^{-\frac{\hat{y}^2}{w_y^2}}\hat{A};$$

$$\text{where} \quad \hat{A} = [\hat{a}e^{-i(k\hat{z}+\Phi(\hat{z}))} + \hat{a}^\dagger e^{+i(k\hat{z}+\Phi(\hat{z}))}] \tag{B5}$$

$$\text{and} \quad E_d = \frac{\alpha\epsilon_c\epsilon_{tw}\sin\theta}{2\hbar}, \tag{B6}$$

while $\phi = kY_0^{(c)}$ represents the effect of the shift between the origin of the tweezer field and the cavity standing wave. Linearising $\hat{V}_{\rm CS}$ about equilibrium displacements yields the optomechanical coupling strengths:

$$g_x \simeq -E_d\, k \sin\theta \sin\phi X_{zpf}, \quad g_y \simeq -E_d\, k \cos\theta \sin\phi Y_{zpf}, \tag{B7}$$

$X_{zpf} = \sqrt{\hbar/(2m\omega_x)}$, $Y_{zpf} = \sqrt{\hbar/(2m\omega_y)}$.

In addition, as a feature of the CS set up, the linearization yields also direct x-y couplings $g_{xy} \simeq -g_x g_y \frac{2{\rm Re}(\bar{\alpha})\cos\phi}{E_d \sin^2\phi}$ related to the mean photon occupancy $n_p = |\bar{\alpha}|^2$ in the cavity. They are negligible at the nodes ($\phi = \pi/2$), but become stronger as $\phi \to 0$.

1. Tweezer trap frequencies

The mechanical x, y frequencies are set mainly by the tweezer trap $-\frac{\alpha}{2}|\hat{\mathbf{E}}_{\rm tw}|^2$. Linearising leads to

$$\left(\omega_{x,y}^{(0)}\right)^2 = \frac{\alpha\epsilon_{tw}^2}{m w_{x,y}^2}. \tag{B8}$$

2. Cotrapping

The linearization of $\hat{V}_{\rm CS}$ also yields corrections to the tweezer trap frequencies: the zero-th order frequency must be corrected by cotrapping by the coherent scattering potential in Eq. (B5). These stiffen the tweezer frequencies by corrections of the form

$$(\delta\omega_x)^2 \simeq \frac{E_d\hbar}{m} 2\alpha_R \cos\phi \left[k^2 \sin^2\theta + \frac{2}{w_x^2}\right],$$
$$(\delta\omega_y)^2 \simeq \frac{E_d\hbar}{m} 2\alpha_R \cos\phi \left[k^2 \cos^2\theta + \frac{2}{w_y^2}\right]. \tag{B9}$$

For the x, y frequencies, the stiffening depends on the mean cavity field:

$$\bar{\alpha} = \alpha_R + i\alpha_I = \frac{-iE_d\cos\phi}{i\Delta - \kappa/2} \tag{B10}$$

so $\alpha_R = \frac{-\Delta E_d \cos\phi}{\kappa^2/4+\Delta^2}$.

We note that the second term in the square brackets in Eq. (B9) is small, so $(\delta\omega_x)^2 \simeq \frac{E_d\hbar}{m} 2\alpha_R \cos\phi k^2 \sin^2\theta$ represents already a good approximation to the frequency correction.

3. Optical spring

A well-studied effect in optomechanics is the so called "optical spring" shift of the mechanical frequencies that arises from the dynamical interplay between the fluctuations in the optical mode and the mechanical motion. If we write the self-energy as $\Sigma(\omega \simeq \omega_j) = -i2g_j^2\omega_j\eta_c(\omega \simeq \omega_j)$, for $j \equiv x, y$, its imaginary part related to the optomechanical damping, while its *real* part is related to the optical spring shift squared:

$$(\delta\omega_{(OS,x)})^2 \simeq \omega_x {\rm Re}\left\{-i2g_x^2\eta_c(\omega=\omega_x)\right\},$$
$$(\delta\omega_{(OS,y)})^2 \simeq \omega_y {\rm Re}\left\{-i2g_y^2\eta_c(\omega=\omega_y)\right\}. \tag{B11}$$

For red detuning, it softens the mechanical frequencies. It is strongest at the node and tends to zero as the antinode is approached. In Ref. [19], an additional correction was found, resulting from the intrinsic 2D dynamics, that here is negligible.

APPENDIX C: THE S_{xy} SPECTRUM

It was shown in Ref. [19] that one can correct the 1D mechanical displacement spectra to allow for hybridization. For the x displacement, for example, one can write

$$\hat{x}^{\rm 3D}(\omega) = \hat{x}^{\rm 1D}(\omega) + \mathcal{R}_{xy}(\omega)\hat{y}^{\rm 3D}(\omega) + \mathcal{R}_{xz}(\omega)\hat{z}^{\rm 3D}(\omega) \tag{C1}$$

using the appropriate hybridization functions, $\mathcal{R}_{jk}(\omega)$, introduced in Ref. [19], to correct the unhybridized spectra, $\hat{x}^{\rm 1D}(\omega)$. Analogous expressions are obtained for y, z. Since the unhybridized spectra are well-known and given in terms of optical noises, the x, y, z expressions can be rearranged and solved in closed form to obtain PSDs and arbitrary correlation spectra. It is assumed that linearization of the equations of motion is valid and we can use quantum linear theory (QLT).

We obtained "exact" QLT PSDs $S_{xx}(\omega)$, $S_{yy}(\omega)$ and correlation spectra $S_{xy}(\omega)$ to compare with experiment. However, for physical insight, we also obtain below a simplified analysis that gives excellent agreement with the full 3D QLT. As the motion is approximately 2D, we neglect the z motion and we further approximate:

$$\hat{x}^{\rm 3D}(\omega) \simeq \hat{x}^{\rm 1D}(\omega) + \mathcal{R}_{xy}(\omega)\hat{y}^{\rm 1D}(\omega), \tag{C2}$$
$$\hat{y}^{\rm 3D}(\omega) \simeq \hat{y}^{\rm 1D}(\omega) + \mathcal{R}_{yx}(\omega)\hat{x}^{\rm 1D}(\omega). \tag{C3}$$

where for a modest hybridization correction, we substitute the 1D expressions in the last term. Below, we drop the 3D superscript and assume that $\hat{x}, \hat{y}$ include hybridization. To compare with experiment, we consider the symmetrized mechanical correlations:

$$S_{xy}(\omega) = \tfrac{1}{2}(\langle[\hat{x}]^\dagger\hat{y}\rangle + \langle[\hat{y}]^\dagger\hat{x}\rangle). \tag{C4}$$

The current experiments are in weak coupling regimes and there is little mechanical-optical hybridization. This means that $\langle[\hat{x}^{1D}]^\dagger\hat{y}^{1D}\rangle \simeq 0$. However, in regimes of strong optical back-actions, even the unhybrized modes can be correlated hence $\langle[\hat{x}^{1D}]^\dagger\hat{y}^{1D}\rangle \neq 0$. We have verified numerically that the 1D components have negligible cross-correlations, so $S_{xy}^{\rm 1D} \simeq 0$ and hence

$$S_{xy}(\omega) \approx ({\rm Re}(\mathcal{R}_{yx}(\omega))S_{xx}(\omega) + {\rm Re}(\mathcal{R}_{xy}(\omega))S_{yy}(\omega)). \tag{C5}$$

We can see that the cross-correlations are closely related to the real part of the hybridization functions. The latter can be given explicitly:

$$\mathcal{R}_{xy}(\omega) = \frac{i\mu_x(\omega)}{M_x(\omega)}G(\omega) \quad \text{and} \quad \mathcal{R}_{yx}(\omega) = \frac{i\mu_y(\omega)}{M_y(\omega)}G(\omega), \tag{C6}$$

where $G(\omega) = [i\eta_c(\omega)g_x g_y + g_{xy}]$ is a term that represents the interference between the "direct" static coupling between x and y (proportional to g_{xy}); and an indirect, cavity mediated, coupling term (proportional to $g_x g_y$). The prefactors

$M_j(\omega) = 1 + g_j^2 \mu_j(\omega)\eta_c(\omega)$ include a small optical back-action correction to each displacement. For our simplified analysis, we take $M_j \simeq 1$. Numerical tests showed this is an excellent approximation. The reason for this is that the small backaction correction is peaked around each of the mechanical frequencies, i.e. at $M_x(\omega \approx \omega_x)$, and $M_y(\omega \approx \omega_y)$ while for the cross-correlation, we show below the values around $M_x(\omega \approx \omega_y) \approx 1$, and $M_y(\omega \approx \omega_x) \approx 1$ are most important.

We note that, in the present discussion, we refer to both the cavity mediated couplings $\eta_c(\omega) g_x g_y$ as well as the usual optomechanical back-action terms $g_j^2 \eta_c(\omega)$ as 'optical back-action' terms, but clearly, in the former case, the optical backaction acts on different mechanical modes.

1. Optical and mechanical susceptibilities

The $\mu_j(\omega)$ are mechanical susceptibilities, while η_c is the optical susceptibility. We have the usual mechanical susceptibility $\mu_j(\omega) = \chi(\omega, \omega_j) - \chi^*(-\omega, \omega_j)$ and optical susceptibility $\eta_c(\omega) = \chi(\omega, -\Delta) - \chi^*(-\omega, -\Delta)$, where e.g. $\chi(\omega, \omega_x) = [-i(\omega - \omega_x) + \frac{\Gamma}{2}]^{-1}$ and $\chi(\omega, \Delta) = [-i(\omega - \Delta) + \frac{\kappa}{2}]^{-1}$

2. Anticorrelation of S_{xy}

We can readily show that the x-y modes are in general anti-correlated (and this was observed in the experimental data) by showing that the hybridization functions $\mathrm{Re}\mathcal{R}_{xy} \approx -\mathrm{Re}\mathcal{R}_{yx}$.

We have shown that $\mathcal{R}_{xy}(\omega) \simeq G(\omega) i\mu_x(\omega)$ and $\mathcal{R}_{yx}(\omega) \simeq G(\omega) i\mu_y(\omega)$ and

$$S_{xy}(\omega) \approx (\mathrm{Re}[i\mu_y(\omega)G(\omega)]S_{xx} + \mathrm{Re}[i\mu_x(\omega)G(\omega)]S_{yy}). \tag{C7}$$

However, the PSDs are sharply peaked about the mechanical frequencies $S_{xx}(\omega \approx \omega_x)$ and $S_{yy}(\omega \approx \omega_y)$, hence we are interested in the value prefactors at those frequencies, namely, $\mu_y(\omega \sim \omega_x)G(\omega \approx \omega_x)$ and $\mu_x(\omega \sim \omega_y)G(\omega \approx \omega_y)$.

Since $\kappa \gg |\omega_x - \omega_y|$, the cavity susceptibility function $\eta_c(\omega)$, and hence $G(\omega)$ is insensitive to frequency: i.e. $G(\omega_x) \sim G(\omega_y)$. Hence the anticorrelation behavior must originate in the mechanical susceptibilities.

However, since $\omega_x + \omega_y \gg |\omega_x - \omega_y|$ and the mechanical damping $\Gamma \ll |\omega_x - \omega_y|$ is negligible at ultrahigh vacuum, we can write

$$\mu_x(\omega \sim \omega_y) \simeq \left[-i(\omega_y - \omega_x) + \frac{\Gamma}{2}\right]^{-1} \simeq i/(\omega_x - \omega_y) \tag{C8}$$

and

$$\mu_y(\omega \sim \omega_x) \simeq \left[-i(\omega_x - \omega_y) + \frac{\Gamma}{2}\right]^{-1} \simeq i/(\omega_y - \omega_x). \tag{C9}$$

Finally, we obtain an approximate expression for the mechanical correlation spectra:

$$S_{xy}(\omega) \approx \frac{G(\omega)}{\omega_x - \omega_y}[S_{yy}(\omega) - S_{xx}(\omega)] \tag{C10}$$

showing clearly that the x and y peaks have opposite signs. So the anticorrelation arises because the susceptibility for y involves upconverting in frequency whereas x represents a down-conversion. The overall sign flips when $G(\omega)$ changes sign. For $\theta = 3\pi/4$ then $g_x = -g_y$ and $g_{xy} \to -g_{xy}$ so there is a global sign flip of S_{xy} relative to $\theta = 3\pi/4$.

Since $G(\omega \sim \omega_x) \simeq G(\omega \sim \omega_y) \equiv G$, the prefactor is a constant and we can equate it to the rotation angle $\Phi \sim \frac{G}{\omega_x - \omega_y}$. Hence, we can write

$$S_{xy}(\omega) \approx \Phi[S_{yy}(\omega) - S_{xx}(\omega)]. \tag{C11}$$

3. Comparisons between experiment and theory

We test Eq. (C11) experimentally by measuring the PSDs $S_{xx}(\omega)$, $S_{yy}(\omega)$ and comparing their difference $S_{yy}(\omega) - S_{xx}(\omega)$ with the measured cross-correlation S_{xy}. Figure 5 shows that the shape of the difference spectrum, rescaled by a constant (green lines) in most cases follows almost perfectly the cross-correlation (black line), validating Eq. (C11) and enabling one to infer Φ experimentally. This procedure was repeated for 44 data sets at different x_0 and two values of detuning Δ to yield the Φ shown in Fig. 2 of the main manuscript.

The curves were also compared with theoretically calculated S_{xx}, S_{yy} and S_{xy} using QLT. The mode rotation angles can be obtained by comparing difference and cross-correlation PSDs or directly from the analytical model $\Phi \sim \frac{G}{\omega_x - \omega_y}$. In practice, a calculation employing the expression $\Phi = \frac{1}{2}(\mathrm{Re}[R_{xy}] - \mathrm{Re}[R_{yx}])$ was used in Fig. 2, but the simplified expressions are generally quite accurate.

However, in Fig. 5, we plot also theoretical PSDs for S_{xx}, S_{yy}, and S_{xy} (red dashed lines). For all datasets, it is assumed that $\theta = 49^\circ$ and input power $P_{\mathrm{in}} = 0.485$ W. For the data points near the nodes and cancellation points, there is excellent agreement with all the experimental PSDs. However, as seen in Fig. 5, the agreement for data points near the antinode is less good.

For the three data points near the antinode, the heights of the theory QLTs were 2–3 times higher than the experimental values: while PSD amplitudes near the node/cancellation give good agreement assuming the estimated gas pressure $P = 3 \times 10^{-3}$ mbar, near the node, the theory curves assume $P = 1$–2×10^{-3} mbar. This has no effect on Φ or the frequencies but suggests there may be some fluctuation in settings leading to a factor 2–3 overestimate in the modeled temperature.

The theory rotation angles remain reasonable even at the antinode: as expected from theory the cross-correlation flip in sign. The frequencies are far more sensitive as the dynamical and static shifts represent only a couple of percent of the mode frequencies. This is apparent in Fig. 5, where there is an $\sim$1 kHz error in $\omega_x/2\pi$, for $\Delta/2\pi = -176$ kHz, near the antinode; while only 1% of the mode frequency, in Fig. 2 of the main text, this appears as a large discrepancy. There is the possibility that the method we are using to change the particle mean position in the cavity field might introduce a small ellipticity and/or a slight increase in aberrations, e.g., coma, which would affect the waist of the tweezer. This is something we are currently investigating. However, the data could be modelled by QLT theory, without discrepancy, by allowing P_{in} and θ to fluctuate slightly from node to antinode.

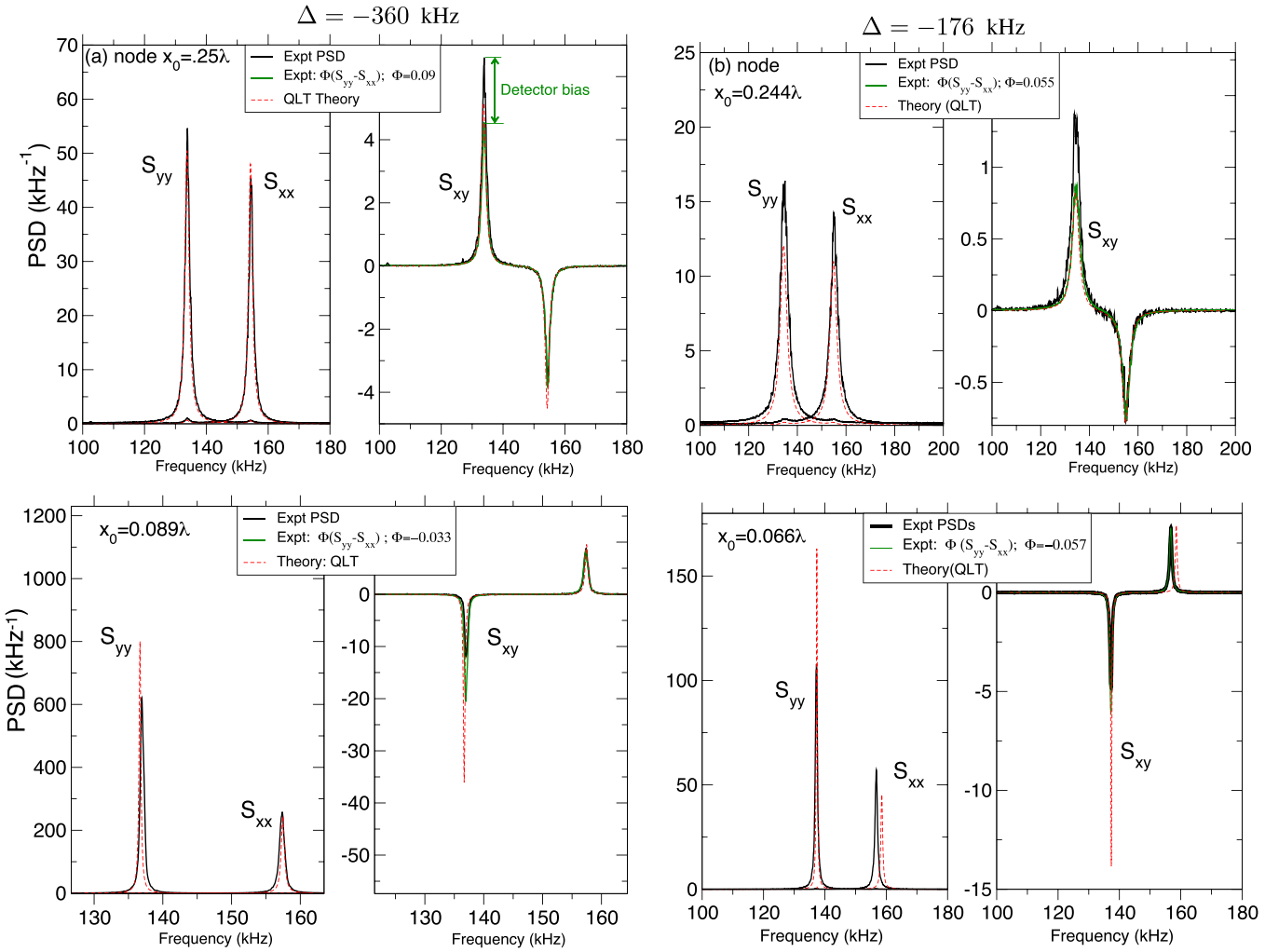

FIG. 5. Experimental data: measuring the mode rotation angle Φ, for different placements (x_0) of the nanoparticle and detunings Δ. Black lines show experimental PSDs, $S_{xx}(\omega)$, $S_{yy}(\omega)$, as well as $S_{xy}(\omega)$. The right panels compare the difference spectrum ($S_{yy} - S_{xx}$) (green lines) and show that it accurately follows the cross-correlation S_{xy} when rescaled by a constant Φ as predicted by Eq. (C11). The red-dashed lines compare with theoretically calculated (QLT) spectra. (a) $\Delta/2\pi = -360$ kHz, nanoparticle at the node. (b) $\Delta/2\pi = -176$ kHz, nanoparticle near the node. For all data at the node or up to the cancellation point, agreement between the cross-correlation (black) and rescaled difference spectra (green) is excellent, except for the detector bias (a systematic $\Phi \approx 0.03$ shift for all y peaks due to misalignment of one detector). Agreement with theoretical QLT (red dash lines) is also good given that no fluctuations whatsoever in assumed parameters were allowed to improve the match. (c) $\Delta/2\pi = -360$ kHz near antinode and (d) $\Delta/2\pi = -176$ kHz near the antinode. shows that for the data close to the antinode, the comparison employing the model Eq. (C11) (green and black lines) remains excellent, so an experimental Φ may be inferred. However, comparison with QLT is less good. In particular, there is an ∼1 kHz discrepancy between the theoretical (QLT, red-dashed line) frequencies and measured frequencies, indicating there may be small fluctuations of experimental parameters over each measurement run.

4. Suppression of hybridization

If the term $G(\omega)[i\eta_c(\omega)g_x g_y + g_{xy}] \simeq 0$, the destructive interference between x-y coupling and indirect, cavity-mode mediated coupling suppresses hybridization and hence $S_{xy} \simeq 0$.

Since the direct coupling $g_{xy} \simeq -g_x g_y \frac{2\mathrm{Re}(\bar{\alpha})\cos\phi}{E_d \sin^2\phi}$, and $\bar{\alpha} \simeq -iE_d \cos(\phi)[i\Delta - \kappa/2]^{-1}$:

$$g_{xy} \simeq g_x g_y \left[\frac{2\Delta \cot^2\phi}{\Delta^2 + \frac{\kappa^2}{4}}\right]. \tag{C12}$$

Thus depending on the positioning, Δ or κ, the direct couplings contribution can be similar or exceed the cavity mediated coupling. Direct and indirect contributions, in general,interfere destructively. We can show that $i\eta_c(\omega) \to \frac{-2\Delta}{(\kappa/2)^2+\Delta^2}$ if -$\Delta \gg \omega$ (and we are interested primarily in the region $\omega \sim \omega_j$). Thus, for large $-\Delta$,

$$G(\omega) \approx g_x g_y \left[\frac{-2\Delta}{\Delta^2 + (\kappa/2)^2}\right][1 - \cot^2\phi], \tag{C13}$$

and we see that the G is real and frequency independent. Furthermore, at $\phi = \pi/4$, the x-y hybridization almost fully vanishes so we have a cancellation point where the S_{xy} correlation spectra are near zero.

APPENDIX D: BEHAVIOR OF $\phi = \phi_c$

In the present experimental study, we are not necessarily in the large detuning limit so we consider other regimes including $-\Delta \sim \omega_{x,y}$ and find the cancellation $\phi = \phi_c$ moves towards the node.

Although the present experimental data is not conclusive, it is certainly consistent with a $\phi_c/2\pi \simeq 0.145$ for $-\Delta/2\pi = 176$ kHz, closer to the node than for $-\Delta/2\pi = 360$ kHz, for which $\phi_c/2\pi \simeq 0.125$. Operating even closer to the node might be more advantageous for quantum optomechanics as it reduces cavity photon occupancies and thus the deleterious effects of optical noise.

We first consider the simplified form of the rotation angle $\Phi(\phi) \sim \frac{G}{\omega_x - \omega_y}$, neglect its frequency dependence and consider its behavior at the single frequency point $\omega = \omega_y$:

$$\Phi(\phi) = \frac{A}{\omega_y - \omega_x}(\mathrm{Re}[i\eta_c(\omega_y)]\sin^2\phi + B\cos^2\phi), \quad \text{(D1)}$$

where $A = \frac{g_x g_y}{\sin^2\phi} = E_d^2 k^2 X_{zpf} Y_{zpf} \sin\theta\cos\theta$ and $B = \frac{g_{xy}}{g_x g_y} = \frac{2\Delta}{\Delta^2 + \kappa^2/4}$.

Solving for $\Phi(\phi_c) = 0$ leads to

$$\phi_c = \tan^{-1}(\sqrt{C_\phi}), \text{ where } C_\phi = -B/\mathrm{Re}[i\eta_c(\omega_y)]. \quad \text{(D2)}$$

Using this simple approach, where we consider cancellation at a single point, we plot Eq. (D2) in Fig. 6, showing how the cancellation point ϕ_c varies with κ and Δ. First, we highlight that the predictions for the two experimentally explored sets of parameters (white dots) match the observation of the cancellation point moving closer to node as the detuning approaches resonance $-\Delta/2\pi = 176\,\mathrm{kHz} \sim \omega_y/2\pi = 136\,\mathrm{kHz}$.

Next, we note that Fig. 6 [and hence Eq. (D2)] verifies that, as C_ϕ gets larger ($\kappa, \Delta \gg \omega_y$), $\phi_c/2\pi \to 0.125$, consistent with the analysis from the previous section.

Equation (D2) also shows that ϕ_c is real-valued as long as $C_\phi \geqslant 0$. Using the cavity susceptibility function $\eta_c(\omega_y)$, we write

$$C_\phi = \frac{(\Delta^2 + \kappa^2/4 - \omega_y^2)^2 + (\kappa\omega_y)^2}{(\Delta^2 + \kappa^2/4 - \omega_y^2)(\Delta^2 + \kappa^2/4)}. \quad \text{(D3)}$$

By inspection, it is seen from the first parentheses in the denominator (other terms being always positive) that $C_\phi \geqslant 0$ holds so long as $\Delta^2 + \kappa^2/4 > \omega_y^2$. This condition is seen clearly in Fig. 6 to be the form of the blank ellipse in the top left, which has a radius in the κ (Δ) axis of $2\omega_y$ (ω_y).

Lastly, the higher-valued area between the $\phi_c/2\pi = 0.2$ and 0.17 contours suggests that—although this particular $\kappa/2\pi = 396\,\mathrm{kHz}$ might be limited to $\phi_c/2\pi \sim 0.17$–0.18 (even in an extreme $-\Delta \ll \omega_y$ limit)—for operation in the good cavity regime, with $\kappa \gtrsim 2\omega_y \simeq 270\,\mathrm{kHz} \cdot 2\pi$, then $\phi_c/2\pi \sim 0.2$ is approached.

APPENDIX E: BEHAVIOR OF Φ

The previous section considered *where* the minimal rotation angle and not the quality of the suppression of Φ. Above we considered only the cancellation at the single frequency point $\omega = \omega_y$, where $G(\omega = \omega_y) = 0$. However, cancellation

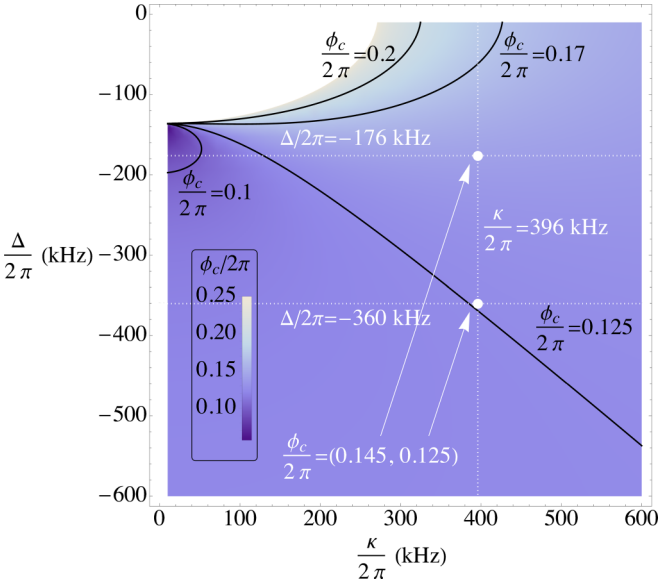

FIG. 6. Density plot of the cancellation point $\phi_c = \tan^{-1}(\sqrt{C_\phi})$ as a function of the cavity linewidth κ and optical detuning Δ, with black contours at notable values. C_ϕ is shown in Eq. (D3). White-dashed lines show the experimental parameters, with white dots representing the two sets of data taken where ϕ_c was investigated. As highlighted by Fig. 2 in the main text, the ϕ_c predictions agree well with experimental observations. The blank ellipse in the top left is the case where $C_\phi < 0$, leading to complex-valued ϕ_c that is not plotted. This condition leads to $\Delta^2 + \kappa^2/4 < \omega_y^2$, showing the ellipse's radii to be $2\omega_y$ and ω_y in the κ and Δ axes, respectively. The large detuning limit of $\phi_c/2\pi \to 0.125$ can be seen in the lower half. The plot suggests that experiments with this cavity ($\kappa = 396\,\mathrm{kHz} \cdot 2\pi \simeq 2.9\,\omega_y$) are limited to $\phi_c/2\pi \sim 0.17$, even in a very small detuning limit $-\Delta \ll \omega_y$. Nevertheless, the higher-valued (brighter) area around the $\phi_c/2\pi = 0.2$ contour suggests that a better cavity with a realistically lower $\kappa \gtrsim 2\omega_y$, may have cancellation closest to the node with $\phi_c/2\pi \sim 0.2$, so long as the detuning is below resonance. However, if the detuning is above resonance, the $\phi_c/2\pi = 0.1$ contour highlights a region where an increasingly perfect cavity $\kappa \ll \omega_y$ may even move ϕ_c toward the antinode.

is only frequency independent as $-\Delta \to \infty$. Elsewhere, a small frequency dependent cross-correlation residual component is left. The frequency dependence enters principally through $\eta_c(\omega)$

We can estimate this quality of the suppression as ϵ relative to the extremal value at the node

$$\epsilon \equiv \frac{\langle \Phi(\omega \simeq \omega_x, \omega_y) \rangle}{\Phi_{\mathrm{node}}} \quad \text{(E1)}$$

thus by considering the ratio of the average value of the residue around the mechanical frequencies normalized by the maximal value at the node.

In Fig. 7, we illustrate this. For the experimental parameters, Φ is suppressed by a ratio of $\epsilon \approx 250$ at $\Delta/2\pi = -360$ kHz and by a ratio of $\epsilon \approx 100$ at $\Delta/2\pi = -176$ kHz. In Ref. [23], we found that this is quite sufficient to expose the effect of, and thus detect, small directional forces. In Fig. 7(b), we compare with a set of parameters where

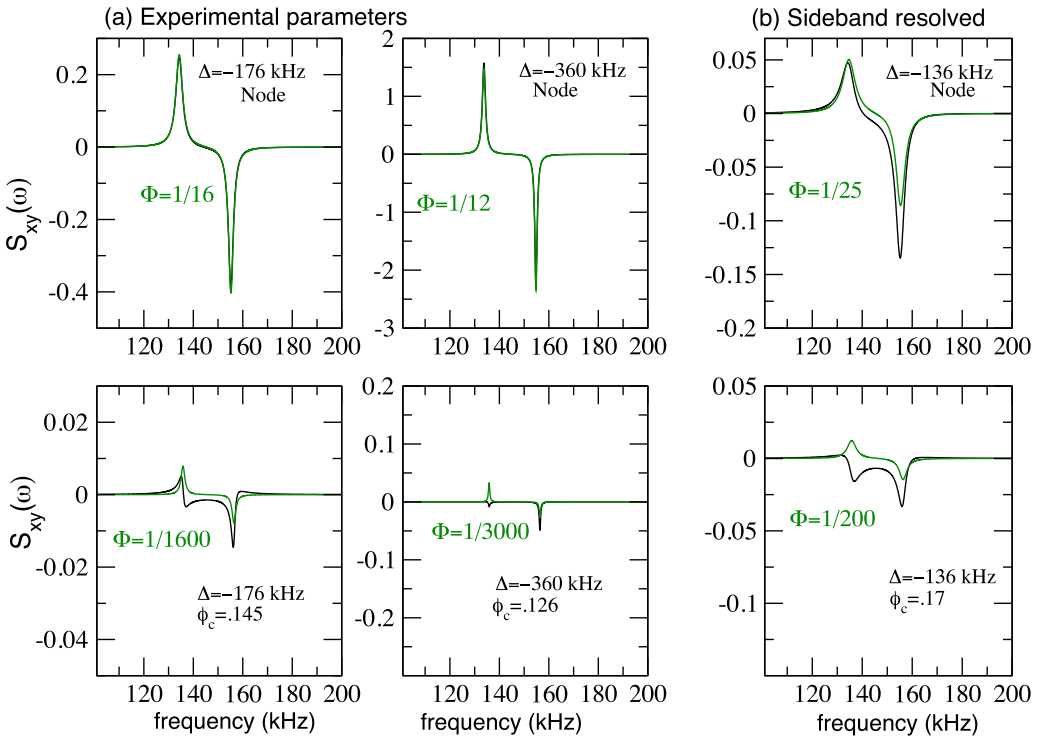

FIG. 7. Compares the accuracy of the suppression of Φ at the node (top panels) relative to the cancellation point ϕ_c. At the cancellation point, a small frequency dependent residue remains. (a) $\Delta/2\pi = -176$ kHz (left). At $\phi_c = 0.145$, the mode rotation Φ is suppressed by a factor $\epsilon \approx 100$ relative to the node (right) $\Delta/2\pi = -176$ kHz; at $\phi_c = 0.126$ the mode rotation is suppressed by a factor $\epsilon \approx 250$ relative to the node . (b) $\Delta/2\pi = -136$ kHz, finesse increased by a factor 1.5 relative to experiments. Now $\phi_c = 0.17$ is significantly closer to the node, but the residue is larger and suppression is only by one order of magnitude. Black lines are cross-correlation spectra, green are the rescaled difference spectra ($\Phi(S_{yy} - S_{xx})$. Note that the small residue at the cancellation points does not in general follow the rescaled PSDs.

$\phi_c = 0.17$ is closer to the node. A slightly higher cavity finesse of $\mathcal{F} = 45\,000$ instead of the 30 000 in the experiments takes the dynamics into the sideband resolved regime. However in this case the suppression is of order $\epsilon \approx 1/8$: nearer the node, the cancellation is still present but gradually degrades as the node is approached.

[1] J. Millen, T. S. Monteiro, R. Pettit, and A. N. Vamivakas, Optomechanics with levitated particles, Rep. Prog. Phys. **83**, 026401 (2020).

[2] A. A. Geraci, S. B. Papp, and J. Kitching, Short-Range Force Detection Using Optically Cooled Levitated Microspheres, Phys. Rev. Lett. **105**, 101101 (2010).

[3] G. Ranjit, M. Cunningham, K. Casey, and A. A. Geraci, Zeptonewton force sensing with nanospheres in an optical lattice, Phys. Rev. A **93**, 053801 (2016).

[4] D. Hempston, J. Vovrosh, M. Toros, G. Winstone, M. Rashid, and H. Ulbricht, Force sensing with an optically levitated charged nanoparticle, Appl. Phys. Lett. **111**, 133111 (2017).

[5] G. Winstone, R. Bennett, M. Rademacher, M. Rashid, S. Buhmann, and H. Ulbricht, Direct measurement of the electrostatic image force of a levitated charged nanoparticle close to a surface, Phys. Rev. A **98**, 053831 (2018).

[6] S. Ahlen, N. AfshordiI, J. B. R. Battat *et al.*, The case for a directional dark matter detector and the status of current experimental efforts, Int. J. Mod. Phys. A **25**, 1 (2010).

[7] F. Mayet, A. M. Green, J. B. R. Battat, J. Billard, N. Bozorgnia, G. B. Gelmini, P. Gondolo, B. J. Kavanagh, S. K. Lee, D. Loomba, J. Monroe, B. Morgan, C. A. J. O'Hare, A. H. G. Peter, N. S. Phan, and S. E. Vahsen, A review of the discovery reach of directional dark matter detection, Phys. Rep. **627**, 1 (2016).

[8] F. Monteiro, G. Afek, D. Carney, G. Krnjaic, J. Wang, and D. C. Moore, Search for Composite Dark Matter with Optically Levitated Sensors, Phys. Rev. Lett. **125**, 181102 (2020).

[9] U. Delić, M. Reisenbauer, K. Dare, D. Grass, V. Vuletić, N. Kiesel, and M. Aspelmeyer, Cooling of a levitated nanoparticle to the motional quantum ground state, Science **367**, 892 (2020).

[10] L. Magrini, P. Rosenzweig, C. Bach, A. Deutschmann-Olek, S. G. Hofer, S. Hong, N. Kiesel, A. Kugi, and M. Aspelmeyer, Optimal quantum control of mechanical motion at room temperature: ground-state cooling, Nature (London) **595**, 373 (2021).

[11] F. Tebbenjohanns, L. Mattana, M. Rossi, M. Frimmer, and L. Novotny, Quantum control of a nanoparticle optically levitated in cryogenic free space, Nature (London) **595**, 378 (2021).

[12] U. Delić, M. Reisenbauer, D. Grass, N. Kiesel, V. Vuletić, and M. Aspelmeyer, Cavity Cooling of a Levitated Nanosphere by Coherent Scattering, Phys. Rev. Lett. **122**, 123602 (2019).

[13] D. Windey, C. Gonzalez-Ballestero, P. Maurer, L. Novotny, O. Romero-Isart, and R. Reimann, Cavity-Based 3D Cooling of a

Levitated Nanoparticle via Coherent Scattering, Phys. Rev. Lett. **122**, 123601 (2019).

[14] V. Vuletić and S. Chu, Laser Cooling of Atoms, Ions, or Molecules by Coherent Scattering, Phys. Rev. Lett. **84**, 3787 (2000).

[15] V. Vuletić, H. W. Chan, and A. T. Black, Three-dimensional cavity doppler cooling and cavity sideband cooling by coherent scattering, Phys. Rev. A **64**, 033405 (2001).

[16] P. Domokos and H. Ritsch, Collective Cooling and Self-Organization of Atoms in a Cavity, Phys. Rev. Lett. **89**, 253003 (2002).

[17] D. R. Leibrandt, J. Labaziewicz, V. Vuletić, and I. L. Chuang, Cavity Sideband Cooling of a Single Trapped Ion, Phys. Rev. Lett. **103**, 103001 (2009).

[18] M. Hosseini, Y. Duan, K. M. Beck, Y.-T. Chen, and V. Vuletić, Cavity Cooling of Many Atoms, Phys. Rev. Lett. **118**, 183601 (2017).

[19] M. Toroš and T. S. Monteiro, Quantum sensing and cooling in three-dimensional levitated cavity optomechanics, Phys. Rev. Res. **2**, 023228 (2020).

[20] M. Toroš, U. Delic, F. Hales, and T. S. Monteiro, Coherent-scattering two-dimensional cooling in levitated cavity optomechanics, Phys. Rev. Res. **3**, 023071 (2021).

[21] A. B. Shkarin, N. E. Flowers-Jacobs, S. W. Hoch, A. D. Kashkanova, C. Deutsch, J. Reichel, and J. G. E. Harris, Optically Mediated Hybridization between Two Mechanical Modes, Phys. Rev. Lett. **112**, 013602 (2014).

[22] A. Ranfagni, P. Vezio, M. Calamai, A. Chowdhury, F. Marino, and F. Marin, Vectorial polaritons in the quantum motion of a levitated nanosphere, Nat. Phys. **17**, 1120 (2021).

[23] A. Pontin and T. S. Monteiro, Towards directional force sensing in levitated optomechanics, arXiv:2208.09065.

[24] A. Ranfagni, K. Borkje, F. Marino, and F. Marin, Two-dimensional quantum motion of a levitated nanosphere, Phys. Rev. Res. **4**, 033051 (2022).

[25] J. Piotrowski, D. Windey, V. Jayadev, C. Gonzalez-Ballestero, A. de los Ríos Sommer, N. Meyer, R. Quidant, O. Romero-Isart, R. Reimann, and L. Novotny, Simultaneous ground-state cooling of two mechanical modes of a levitated nanoparticle, arXiv:2205.10193.

[26] M. Abdi, Sh. Barzanjeh, P. Tombesi, and D. Vitali, Effect of phase noise on the generation of stationary entanglement in cavity optomechanics, Phys. Rev. A **84**, 032325 (2011).

[27] P. Rabl, C. Genes, K. Hammerer, and M. Aspelmeyer, Phase-noise induced limitations on cooling and coherent evolution in optomechanical systems, Phys. Rev. A **80**, 063819 (2009).

[28] J. Schäfer, H. Rudolph, K. Hornberger, and B. A. Stickler, Cooling Nanorotors by Elliptic Coherent Scattering, Phys. Rev. Lett. **126**, 163603 (2021).

[29] A. Pontin, H. Fu, M. Toroš, T. S. Monteiro, and P. F. Barker, Simultaneous cooling of all six degrees of freedom of an optically levitated nanoparticle by elliptic coherent scattering, arXiv:2205.10193.